Appl. Magn. Reson. 30, 311–327 (2006)

Applied Magnetic Resonance

© Springer-Verlag 2006
Printed in Austria

Absolute Signs of Hyperfine Coupling Constants as Determined by Pulse ENDOR of Polarized Radical Pairs

B. Epel[1], J. Niklas[1], M. L. Antonkine[1,2,*], and W. Lubitz[1]

[1] Max-Planck-Institut für Bioanorganische Chemie, Mülheim an der Ruhr, Germany
[2] Institut für Experimentalphysik, Freie Universität Berlin, Berlin, Germany

Received August 18, 2006; revised September 8, 2006

Abstract. A novel method that allows the determination of absolute signs of hyperfine coupling constants in polarized radical pair (RP) pulse electron–nuclear double resonance (ENDOR) spectra is presented. The variable mixing time (VMT) ENDOR method used here leads to a separation of ENDOR transitions originating from different electron spin manifolds by employing their dependence on the time-dependent parameters of the pulse sequence. The simple kinetic model of the RP VMT ENDOR experiment shows very good agreement with the experiments performed on the $P_{700}^{+}A_1^{-}$ RP in photosystem I. This method relies on the selective excitation of absorptive or emissive lines of one radical in the RP EPR spectrum and therefore requires high spectral resolution. This condition was fulfilled for the system studied at the low-field edge of the RP EPR spectrum obtained at Q-band. The method presented here has a very high sensitivity and does not require any equipment additional to the one used for RP pulse ENDOR. The VMT ENDOR method offers the possibility for selective suppression of signals from different electron spin manifolds.

1 Introduction

Electron–nuclear double resonance (ENDOR) spectroscopy is an important tool for the characterization of electron-nuclear hyperfine (hf) interactions in paramagnetic systems [1–4]. ENDOR spectroscopy has been widely applied for the study of photosynthetic reaction centers (RCs) (for a recent review see ref. 5). Pulse ENDOR spectroscopy on short-lived intermediates, e.g., radical pairs (RPs) is of particular interest since it provides information on the initially formed species in the process of charge separation [5–10]. Due to the transient nature and the polarization of electron spin states, such signals are very strong and can easily be differentiated from stationary signals.

* On leave from Photochemistry Center, Russian Academy of Sciences, Moscow, Russian Federation

The ENDOR spectra provide the magnitude of the hf coupling constants (hfcc) but do not directly give their signs. It is known that nuclei can have different signs of hf couplings, depending on the interaction mechanism [11]. Especially important is the sign of the isotropic coupling (A_{iso}), which depends on the mechanism leading to a nonzero electron spin density at the nucleus. For α-protons in π-radicals, which are coupled by the exchange mechanism (π-σ spin polarization), a negative sign of A_{iso} is typically found, while a positive sign is an indication of the hyperconjugation mechanism and characteristic for β-protons as found in methyl or methylene groups. Deviations from this rule are found for small hfccs due to π-π polarization in the π-system of the radical [3, 12]. Hence, the sign of the hfcc contains important information which is required for an in-depth analysis of the ENDOR spectra of radicals.

There are several methods of hfcc sign determination. The majority of them provides only the relative signs of two hfcc with respect to each other. Most commonly used is the electron-nuclear-nuclear TRIPLE experiment [2, 13–16]. By this method the correlation between the nuclear transition frequencies of different nuclei is established, which leads to the determination of the relative signs of their hfccs. TRIPLE is successfully applied in liquids [2, 3, 17], whereas in frozen solutions and powder samples it typically suffers from lower sensitivity [4], which makes its application somewhat problematic for the measurements on the short-lived intermediates. Sometimes it is possible to determine the absolute sign of an hfcc by analysis of the shape of ENDOR lines (e.g., in case of an axial hf tensor) [11]. Under certain conditions the sign of the hfcc can be determined in polarized RP ENDOR experiments [8]. However, only the relaxation-based methods provide a solid experimental basis for the determination of the absolute sign of the hfcc as recently demonstrated by Epel et al. [18, 19].

Pulse ENDOR of strongly coupled protons is typically measured by the Davies ENDOR sequence (Fig. 1) [20]. The sequence can be separated into three periods: the inversion, mixing and detection period. The first microwave (MW) π-pulse selectively inverts the population of the electron spin levels. The subsequent radiofrequency (RF) π-pulse is mixing transitions with different projections of nuclear spins. Then the detection sequence (e.g., two-pulse Hahn echo, as shown in Fig. 1) monitors the resulting populations of the electron spin levels. The ENDOR spectrum is obtained by scanning the RF frequency. For investigation of light-induced signals such as those arising from RPs, the sequence is preceded by a laser flash.

The pulse TRIPLE sequence (analogous to the continuous wave general TRIPLE experiment) is similar to the Davies ENDOR sequence with the addition of a second RF pulse (Fig. 1) [15]. In the TRIPLE experiment one of the RF pulses excites the transition belonging to one nucleus while the frequency of the other RF pulse is swept. The difference TRIPLE spectrum is obtained by subtraction of the TRIPLE spectrum from the Davies ENDOR spectrum.

A modification of the Davies ENDOR sequence, which allows the determination of absolute signs of hfcc was recently proposed [18, 19]. It was found that in the case of strong polarization of electron spin states (e.g., at high fields

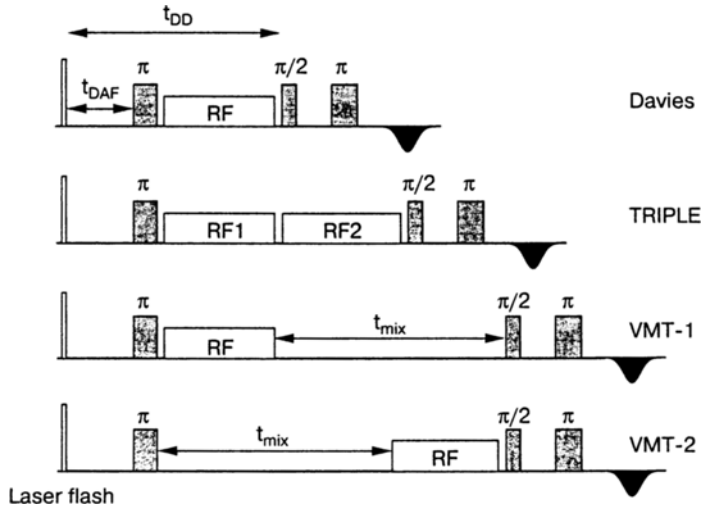

Fig. 1. Davies ENDOR, TRIPLE, VMT-1 and VMT-2 ENDOR pulse sequences; π and π/2 refer to the MW pulses; RF, RF1 and RF2 denotes the RF π-pulses; t_{DAF} is the delay after the laser flash to the first pulse of the sequence; t_{DD} is the delay after the laser flash to the detection sequence; t_{mix} is the additional mixing time used in the VMT experiments.

and low temperatures) the introduction of an additional delay time t_{mix} after the RF pulse (see variable mixing time [VMT]-1 sequence, Fig. 1), comparable with the electron spin lattice relaxation time, results in a change of the relative intensities of ENDOR lines originating from different electron spin manifolds. This change of intensities allows to assign the ENDOR lines to the electron spin manifold and in turn to determine the sign of the hfcc. Although the experimental conditions are different from refs. 18 and 19, similar effects are expected for a RP due to the strong nonequilibrium polarization of the electron spin states of the RP.

In this communication we introduce a new experimental method for the sign determination of hfccs, using the difference in the relaxation behavior of ENDOR transitions in different electronic manifolds of a RP. As system we chose photosystem I (PS I). Upon light excitation at low temperature, a reversible charge separation is generated in PS I, creating the spin-correlated RP $P_{700}^{\bullet+}A_1^{\bullet-}$. The electron donor P_{700} is a chlorophyll *a*/*a'* heterodimer, while the acceptor A_1 is a quinone molecule (vitamin K_1) [21–23].

2 Materials and Methods

The wild-type strain of the thermophilic cyanobacterium *Thermosynechococcus elongatus* (formerly *Synechococcus elongatus*) was grown under continuous white light. Growth and isolation of trimeric PS I was done as described previously

[24]. Crystals of PS I trimers were resuspended in buffer containing 20 mM morpholineethanesulfonic acid sodium salt, pH 6.4, 20 mM $MgSO_4$, and 0.02% β-dodecyl-maltoside. The final PS I concentration of the sample was approximately 150 μM. Sodium ascorbate was added to a final concentration of 5 mM in order to produce open RCs ready for charge separation. Afterwards the sample was relaxed for 5 min in the dark at 4 °C and quickly frozen in liquid nitrogen.

The experiments were carried out on a Q-band Bruker ELEXSYS E580-Q spectrometer with a Super Q-FT MW bridge equipped with a homebuilt resonator similar to that in ref. 25. The resonator contains slits to allow in situ light excitation of the sample. Light excitation at 532 nm was achieved with the Brilliant Laser system from Quantel with an output energy of about 12 mJ, operating with 10 Hz repetition rate. All experiments were done at 80 K.

The pulse EPR spectrum has been recorded using the two-pulse sequence 40 ns-τ-80 ns-τ-echo with $\tau = 400$ ns and $t_{DAF} = 1$ μs. ^{1}H ENDOR (similar parameters have been used for VMT-1 and VMT-2 ENDOR) has been recorded using the Davies ENDOR sequence (π-t-$\pi/2$-τ-π-τ-echo) [20] with an MW inversion pulse of $t_\pi = 200$ ns, RF π-pulse of 9 μs, MW pulses of $t_{\pi/2} = 40$ ns, $t_\pi = 80$ ns and $\tau = 400$ ns. In all experiments an additional 3 μs delay has been introduced after the RF pulse to avoid unnecessary noise during the echo detection. In the following, this delay is considered as part of the RF pulse and is not included in the reported t_{mix} value. The generation of RF pulses and the detection were done by an external PC equipped with the SpecMan control program [26] and an Agilent E4420B RF synthesizer. All EPR, ENDOR spectra and time traces were corrected for the "dark" background spectra recorded 10 ms after the laser flash. An RF amplifier (Amplifier Research, type AR2500L) with a maximum output power of 2.5 kW was used. The accumulation time of all ENDOR experiments was about 1 h. The accumulation time for the difference TRIPLE experiment was about 2 h (1 h for the reference Davies ENDOR and 1 h for the TRIPLE experiment). For a comparison of different pulse sequences, it is convenient to define the delay between laser flash and the beginning of the pulse sequence t_{DAF}, and the delay between the laser flash and the detection sequence t_{DD} (Fig. 1).

Two experiments were used for the determination of the relaxation parameters of the RP: (i) the dependence of the two-pulse Hahn echo on t_{DAF} and (ii) inversion recovery. The lengths of the corresponding MW pulses and the MW power used in these experiments were identical to those of the ENDOR experiments. The inversion recovery sequence contained an MW π-pulse delayed by 1 μs after the laser flash and the two-pulse detection sequence delayed by the time t_{DD} after the laser flash.

For simulations of the $P_{700}^{\bullet+}A_1^{\bullet-}$ RP EPR spectrum the program of Salikhov and coworkers [27, 28] was used.

3 Theory

In photosynthetic RCs the charge separation is initiated by light excitation of the electron donor P. P is oxidized and transfers one electron to the electron acceptor Q, leaving it singly reduced (intermediate electron acceptors are neglected)

$$PQ \xrightarrow{h\nu} {}^1P^*Q \rightarrow {}^1(P^{\bullet+}Q^{\bullet-}) \overset{\omega_{ST}}{\rightleftharpoons} {}^3(P^{\bullet+}Q^{\bullet-}) . \quad (1)$$

The fast charge separation, starting from the excited singlet state $^1P^*$, creates an RP in a spin-correlated state with antiparallel electron spins. As a consequence of this peculiar mechanism, the population of the states in the RP deviates strongly from thermal equilibrium.

The energy scheme of two interacting radicals in a magnetic field exhibits four electronic states, which can be described in terms of wavefunctions of singlet and triplet states: $|1\rangle = |T_{+1}\rangle$, $|2\rangle = a^*|S\rangle + b^*|T_0\rangle$, $|3\rangle = -b^*|S\rangle + a^*|T_0\rangle$ and $|4\rangle = |T_{-1}\rangle$ (Fig. 2a) [7, 29]. $|S\rangle$, $|T_{+1}\rangle$, $|T_0\rangle$, and $|T_{-1}\rangle$ are the singlet and triplet

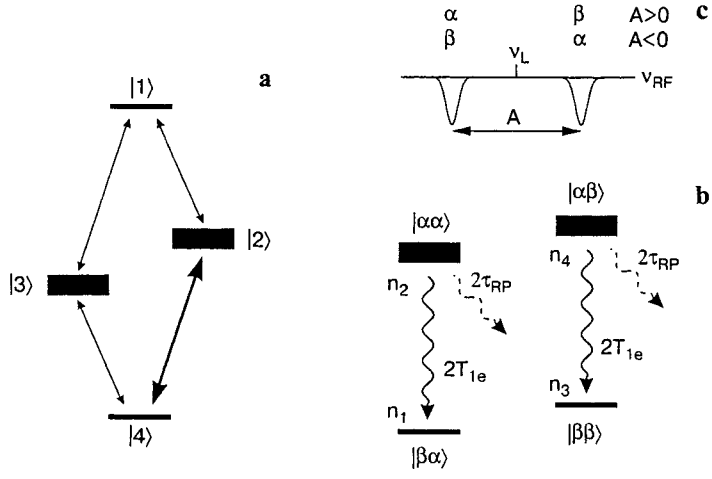

Fig. 2. **a** Electronic energy level scheme for a spin-polarized coupled $S_1 = 1/2$, $S_2 = 1/2$ spin system. The thickness of bars represents the population of the respective levels. The arrows mark the single quantum transitions. The EPR transition considered in this work ($|2\rangle \leftrightarrow |4\rangle$) is marked with a thick arrow. **b** Energy level scheme for the electronic levels α ($|2\rangle$) and β ($|4\rangle$) and the nuclear spin $I = 1/2$ interacting with one of the electron spins. The first symbol in the state description is the electronic state, while the second one relates to the nuclear spin. The nuclear spin projections equal to $+1/2$ and $-1/2$ are marked with α and β, respectively. The populations of the levels are denoted by n_i ($i = 1$–4). The main relaxation pathways are indicated. T_{1e} is the electron spin–lattice relaxation time and τ_{RP} is the RP lifetime (charge recombination time). The latter refers to the electronic state which is partially singlet (α-manifold). **c** Schematic representation of RP ENDOR spectra, corresponding to the level diagram presented in panel b. The weak hf coupling case $|A/2| < \nu_L$ is shown. Here A is the hfcc and ν_L is the nuclear Larmor frequency. The position of ENDOR lines from the α and β electronic manifolds is shown for the case of a positive and a negative hfcc. Both ENDOR lines are in emission.

basis states. Directly after creation of the RP, only those states that carry singlet character (states $|2\rangle$ and $|3\rangle$) are populated. In case of a weakly coupled RP, the states $|2\rangle$ and $|3\rangle$ are equally populated. The pure triplet states (states $|1\rangle$ and $|4\rangle$) are initially empty [7, 29]. Due to the nonequilibrium population of states, the positive (absorptive) and negative (emissive) EPR signals are observed (Fig. 2a) [29–32].

In addition to the spin polarization, the RP exhibits an electron-electron zero-quantum coherence, which oscillates at the frequency ω_{ST} determined by the strength of the coupling between the two spins and the difference in their resonance frequencies, see Eq. (1) [32, 33]. This zero-quantum coherences dephase in the sub-microsecond range in protonated RCs [34, 35]. Since in all experiments in this work the delay after the laser flash (t_{DAF}) was ≥ 1 μs, these zero-quantum coherences do not need to be considered here.

A rigorous treatment of the RP ENDOR experiment is presented in ref. 8. For the calculation of the RP ^{1}H ENDOR spectra, Fursman et al. [8] considered a single nucleus with the spin $I = 1/2$ coupled to one of the two electron spins. The interaction with this nucleus splits all electronic levels in Fig. 2a into two levels that correspond to the projections of the nuclear spin $m_I = +1/2$ and $m_I = -1/2$. In the following, the nuclear spin projections equal to $+1/2$ and $-1/2$ are marked with α and β, respectively. It was demonstrated that the RP ENDOR spectra strongly depend on the difference between the resonance frequencies of the electron spins of the donor and the acceptor ($q = \nu_P - \nu_Q$), the interaction between these electron spins (here we consider only the dipolar part, D) and the hf couplings of nuclei of the corresponding radicals, A. Two different cases can be considered: (i) the strong coupling case $|q| \leq |A|$ and/or $|q| \leq |D|$ and (ii) the weak coupling case $|q| \gg |A|$ and $|q| \gg |D|$. For different orientations of the molecules with respect to the magnetic field, both cases can be observed since q (proportional to the difference of g-factors of the two radicals), D and A are orientation-dependent. The first case corresponds to RP ENDOR spectra measured at a position of the magnetic field where the EPR spectra of both radicals overlap. Then, as was shown in ref. 8, the polarization pattern of the RP ENDOR spectra, in particular, depends on the sign of the hfcc. The mixture of the singlet and triplet states gives rise to additional ENDOR transitions between states $|2\rangle$ and $|3\rangle$. However, in many cases the detailed analysis of the resulting RP ENDOR spectra is only possible for a few specific ENDOR lines (the overlap of the ENDOR patterns from both radicals significantly decreases the spectral resolution). Moreover, the spectra are further complicated by the presence of signals from molecules differently oriented with respect to the magnetic field (powder pattern).

In contrast, ENDOR spectra recorded at magnetic fields where the EPR spectra of the two radicals do not overlap can be treated as the weak coupling case. Especially good spectral resolution can be achieved at magnetic fields where absorptive and emissive EPR transitions of the RP do not overlap (on the low- and high-field edges of the RP EPR spectra). At these magnetic fields, single-crystal-like ENDOR spectra are observed and RP ENDOR spectra are very close

to those of an isolated radical. However, no polarization in the RP ENDOR spectrum due to the sign of hfcc is found [8]. For the observation of the weak coupling case, it is of advantage to use higher EPR frequencies, since q increases with increase of the EPR frequency.

In the following, we consider the extremely weak coupling case and calculate the polarization of ENDOR spectra recorded at an emissive EPR transition (transition $|2\rangle \leftrightarrow |4\rangle$, Fig. 2a). As mentioned above, in the complete system there are a number of ENDOR transitions that belong to electron levels $|1\rangle$, $|2\rangle$, $|3\rangle$ and $|4\rangle$ and partially allowed transitions between levels $|2\rangle$ and $|3\rangle$. However, in our case the ENDOR transitions related to EPR transition $|1\rangle \leftrightarrow |3\rangle$ are not observed and the probability of ENDOR transitions between levels $|2\rangle$ and $|3\rangle$ is very small [8]. Therefore, we can restrict our model to the electronic levels $|2\rangle$ and $|4\rangle$. Taking into account one nucleus with $I = 1/2$, a four-level scheme can be drawn (Fig. 2b). By analogy with an $S = 1/2$ system, the electronic levels $|2\rangle$ and $|4\rangle$ are marked with α and β, respectively. The nonequilibrium population of the RP leads to a state, in which only the levels in the electronic α manifold are initially populated [29]. According to the kinetic model suggested by Timmel et al. [36] for the photosynthetic bacterial RC, the dynamics of spin level populations of the RP are described by two parameters: the RP lifetime (charge recombination time) τ_{RP} and the spin–lattice relaxation time T_{1e}. The first one describes the irreversible annihilation of the RP, which leads to a decrease of the total spin population. Only the states which have a contribution of the singlet $|S\rangle$ state (here states in the electronic α manifold, states $|2\rangle$ and $|3\rangle$ of the complete system) are subject to this mechanism. The states with pure triplet character (here states in the electronic β manifold, states $|1\rangle$ and $|4\rangle$ of the complete system) do not decay directly due to charge recombination, since direct recombination to the singlet ground state PQ is spin-forbidden. The electron spin–lattice relaxation brings the populations of electron levels α and β to thermal equilibrium.

The schematic ENDOR spectrum corresponding to the energy level diagram of Fig. 2b is presented in Fig. 2c. It consists of two lines centered around the nuclear Larmor frequency ν_L, spaced by the effective hfcc, A. Here we assume the weak electron–electron and the weak hf coupling ($|A/2| < \nu_L$) case. Due to the negligible hf enhancement factor for ^{1}H nuclear transitions at Q-band, the amplitudes of stationary ENDOR lines are almost equal.

In the following, we calculate the populations of the levels and consequently the amplitudes of the ENDOR lines as a function of pulse sequence parameters. For the calculations we use the matrix formalism presented by Epel et al. [18]. The system shown in Fig. 2b is mathematically identical to the system described in ref. 18. The population of the corresponding states can be expressed as a vector $\vec{n} = [n_1, n_2, n_3, n_4]$, where n_1, n_2, n_3, and n_4 are the populations of the states $|\beta\alpha\rangle$, $|\alpha\alpha\rangle$, $|\beta\beta\rangle$, and $|\alpha\beta\rangle$, respectively (the numbering of the energy levels is kept similar to ref. 18). The initial population of RP levels is $\vec{n}_0 = \vec{n}\,(t_{DD} = 0) = [0,0.5,0,0.5]$. The sum of the initial populations is equal to 1. The relaxation processes in the four-level system can be described by the operator $\exp(-\Gamma t)$,

where t is the time and Γ is a 4×4 relaxation matrix. The elements of the relaxation matrix depend on electron (T_{1e}) and nuclear (T_{1n}) spin–lattice relaxation, cross-relaxation times (T_x) and the electronic state polarization $f_B = \exp[-h\nu/(kT)]$ (see ref. 18 for the exact definition of the matrix), where k is the Boltzmann constant and T is the temperature in kelvin. To represent the decay of the RP due to charge recombination, we introduce the additional relaxation operator $\exp(-\Gamma_{RP}t)$. This operator describes the irreversible loss of the population of states which have a contribution of the singlet $|S\rangle$ state (states $|\alpha\alpha\rangle$ and $|\alpha\beta\rangle$). The matrix Γ_{RP} has only two nonzero elements $\Gamma_{2,2} = \Gamma_{4,4} = 1/(2\tau_{RP})$, where τ_{RP} is the lifetime of the RP states, which are partially singlet. In the Davies ENDOR experiment, only one of the electron transitions is excited by the MW inversion pulse (here we take the transition $|\beta\alpha\rangle \leftrightarrow |\alpha\alpha\rangle$) [4]. For the case considered here, the choice of the transition is arbitrary and does not affect the calculated ENDOR and VMT ENDOR intensities. The MW π-pulse, described by the operator P^{12} [18], exchanges the populations of the levels $|\beta\alpha\rangle$ and $|\alpha\alpha\rangle$. The RF π-pulses affecting the nuclear transitions in the α and β manifolds are presented by the operators P^{α}_{RF} and P^{β}_{RF} [18]. The length of MW and RF pulses is considered to be negligible.

Three cases have to be considered for hypothetical ENDOR spectra consisting of one line pair: (i) when the RF frequency does not match any of the ENDOR transitions (the baseline, bl) and when it hits a transition either in the (ii) α or (iii) β electron manifolds. The corresponding populations will be denoted with indexes bl, α and β. Since different ENDOR sequences have different parameters of the sequence, for a comparison it is convenient to define the delay time between the laser flash and the beginning of the detection part of the sequences, t_{DD}. For the Davies ENDOR sequence, under the assumption of negligible duration of MW and RF pulses as compared to t_{DAF}, this delay is approximately equal to t_{DAF}. The population of levels after the Davies ENDOR sequence is given by

$$\vec{n}^{bl}(t_{DD} \approx t_{DAF}) = P^{12} \exp[-(\Gamma + \Gamma_{RP})t_{DAF}]\vec{n}_0 , \tag{2a}$$

$$\vec{n}^{\alpha}(t_{DD} \approx t_{DAF}) = P^{\alpha}_{RF} P^{12} \exp[-(\Gamma + \Gamma_{RP})t_{DAF}]\vec{n}_0 , \tag{2b}$$

$$\vec{n}^{\beta}(t_{DD} \approx t_{DAF}) = P^{\beta}_{RF} P^{12} \exp[-(\Gamma + \Gamma_{RP})t_{DAF}]\vec{n}_0 . \tag{2c}$$

The Davies ENDOR signal intensity is calculated according to

$$I^{\alpha,\beta}_{ENDOR} = (n_1^{\alpha,\beta} - n_2^{\alpha,\beta}) - (n_1^{bl} - n_2^{bl}) . \tag{3}$$

Here $n_1^{\alpha,\beta} - n_2^{\alpha,\beta}$ is the signal amplitude when the RF pulse matches one of the ENDOR transitions and $n_1^{bl} - n_2^{bl}$ is the signal amplitude when the RF pulse does not match any transition (baseline). For the calculation of the populations during the VMT-1 ENDOR experiment the formulae

$$\vec{n}^{bl}(t_{DD} \approx t_{mix}) = \exp[-(\Gamma + \Gamma_{RP})t_{mix}]P^{12}\vec{n}_0\,, \tag{4a}$$

$$\vec{n}^{\alpha}(t_{DD} \approx t_{mix}) = \exp[-(\Gamma + \Gamma_{RP})t_{mix}]P^{\alpha}_{RF}P^{12}\vec{n}_0\,, \tag{4b}$$

$$\vec{n}^{\beta}(t_{DD} \approx t_{mix}) = \exp[-(\Gamma + \Gamma_{RP})t_{mix}]P^{\beta}_{RF}P^{12}\vec{n}_0 \tag{4c}$$

were used. Here the RF pulses come at the beginning of the sequence after the MW inversion pulse and the detection is delayed by the time t_{mix}. In VMT experiments the delay t_{DD} is approximately equal to t_{mix}. The VMT ENDOR signal intensities are calculated according to Eq. (3).

4 Results and Discussion

The experimental pulse EPR spectrum of the $P^{\bullet+}_{700}A^{\bullet-}_1$ RP in PS I of *T. elongatus* at Q-band is presented in Fig. 3a. The respective calculated spectrum is shown in Fig. 3b. The simulation parameters are taken from ref. 37. The separate contributions to this spectrum from $A^{\bullet-}_1$ and $P^{\bullet+}_{700}$ radicals are presented in Fig. 3c. It can be seen that due to the much larger anisotropy of the $A^{\bullet-}_1$ g-tensor compared to the $P^{\bullet+}_{700}$ g-tensor, the low-field part of the RP EPR spectrum results only from transitions related to $A^{\bullet-}_1$ (Fig. 3c).

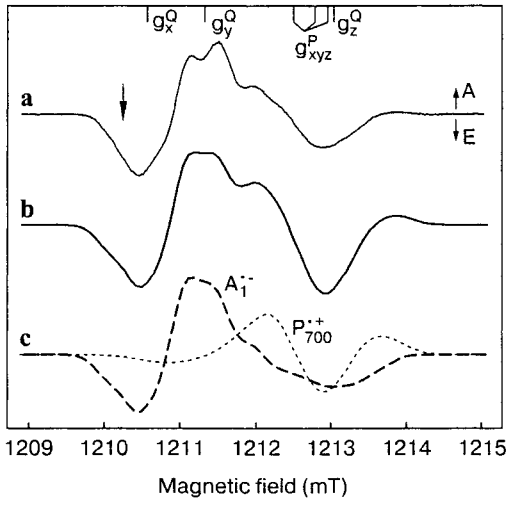

Fig. 3. a Pulse Q-band EPR spectrum of the spin polarized RP $P^{\bullet+}_{700}A^{\bullet-}_1$ in PS I (ν_{MW} = 34.0 GHz, T = 80 K, t_{DAF} = 1 μs, sequence: 40 ns-τ-80 ns-τ-echo with τ = 400 ns). On top the principal values of the g-tensors of the individual radicals (g^Q_i for $A^{\bullet-}_1$; g^P_i for $P^{\bullet+}_{700}$) are given. The magnetic field at which all ENDOR, VMT and TRIPLE experiments were performed is marked with an arrow. **b** Simulation of the RP EPR spectrum. The simulation parameters are taken from ref. 37. **c** Individual contributions of $P^{\bullet+}_{700}$ and $A^{\bullet-}_1$ radicals to the simulated EPR spectrum. The simulation shows that in the ENDOR experiment only the part of the EPR spectrum that belongs to $A^{\bullet-}_1$ is excited.

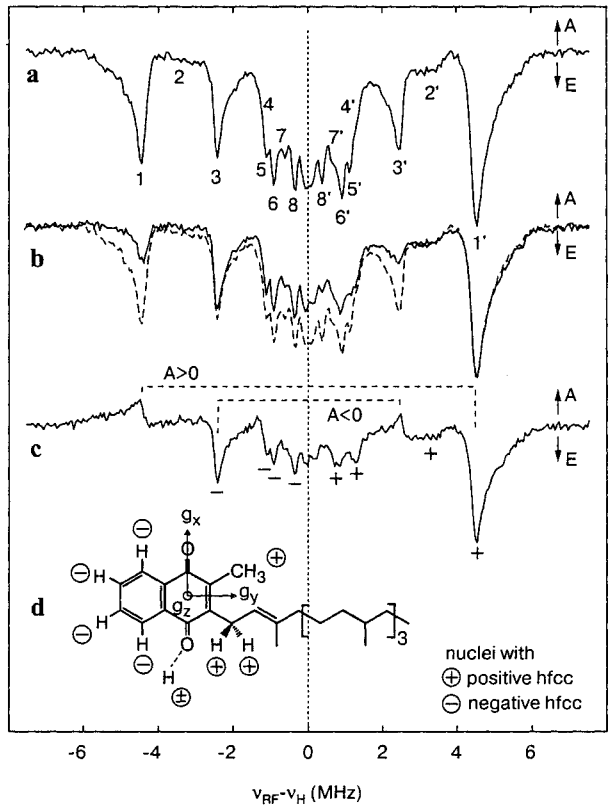

Fig. 4. **a** Q-band Davies ^{1}H ENDOR spectrum of the spin polarized RP $P^{\bullet}_{700}{}^{+}A_1^{\bullet-}$ in PS I (t_{DAF} = 1 μs, t_{DD} = 14 μs) showing at least eight distinct line pairs. **b** RP VMT-1 ENDOR spectrum (t_{DAF} = 1 μs, t_{DD} = 54 μs, solid line) and Davies ENDOR spectrum from trace a (dashed line). Note difference between the ENDOR and VMT line intensities. **c** RP VMT-1 ENDOR spectra (t_{DAF} = 1 μs, t_{DD} = 134 μs). The absolute signs of the hf couplings are given on the corresponding emissive lines. All spectra were recorded at a magnetic field close to g_x^Q (Fig. 3a). Experimental conditions: ν_{MW} = 34.0 GHz, T = 80 K. **d** Molecular structure of VK_1 with g-tensor axes system. The proton of the strong H-bond to the protein is shown as well [23]. Only the protons that are expected to have a distinct contribution to the ENDOR spectra are shown together with the expected signs of the respective hfcc.

Figure 4a–c presents Q-band ^{1}H Davies RP ENDOR and RP VMT ENDOR spectra. The field position on which all experiments were performed is marked with an arrow in Fig. 3a. For the $P^{\bullet+}_{700}A_1^{\bullet-}$ RP in PS I the separation between emissive and absorptive lines in the low-field region of the RP EPR spectrum is about 9.5 MHz and is larger than the isotropic EPR line width of about 8 MHz [37]. Therefore, one can expect that the contribution of the absorptive EPR transition ($|1\rangle \leftrightarrow |3\rangle$) to the ENDOR spectra recorded at this magnetic field is very small. The molecular structure of vitamin K_1 (A_1) is given in Fig. 4d. Note that the field position (close to g_x) selects almost exclusively molecules with their x-

axis (parallel to the C=O bond) aligned along the field direction. Consequently single-crystal-like ENDOR spectra on this position of the magnetic field are expected.

Figure 4a shows the Davies ENDOR spectrum (t_{DAF} = 1 μs, t_{DD} = 14 μs). All lines are emissive (negative) and belong to the $A_1^{\bullet-}$ radical (see, for example, refs. 9 and 38). The amplitudes of ENDOR lines with frequencies larger and smaller than the proton Larmor frequency ν_H are nearly identical (some small asymmetry results from the spectrometer setup, partial excitation of the absorptive EPR transition and VMT effect due to the finite length of RF pulses).

The VMT-1 ENDOR spectrum recorded with t_{DAF} = 1 μs, t_{mix} = 40 μs (t_{DD} = 54 μs) is presented in Fig. 4b (solid line). The Davies ENDOR spectrum (the same as in Fig. 4a), normalized to the amplitude of the VMT-1 ENDOR spectrum, is presented in the same trace (dashed line) for comparison. It is clearly visible that the frequencies of the transitions and the general shapes of lines in the VMT-1 ENDOR and Davies ENDOR spectra are the same. However, the amplitudes of the lines are different. Figure 4c shows the VMT-1 ENDOR spectrum recorded with t_{DAF} = 1 μs, t_{mix} = 123 μs (t_{DD} = 134 μs). Here the effect of the ENDOR amplitude alteration is even more pronounced. Note that the intensities of Davies and VMT ENDOR spectra were not scaled, and spectra were only shifted vertically for better visualization. The VMT ENDOR experiment was also performed with t_{DD} up to 254 μs (not shown). The VMT ENDOR spectrum was similar to the one recorded with t_{DD} = 134 μs with lower intensity and more prominent intensity alteration effect.

The RP VMT ENDOR sequence starts directly after charge separation and takes considerable time. During this time an electron spin density redistribution may occur, as was discussed for bacterial photosynthetic RCs [39]. This may affect the ENDOR spectra. We performed Davies ENDOR experiments with t_{DAF} ranging from 1 to 240 μs (t_{DD} up to 254 μs). The amplitudes of Davies ENDOR spectra recorded with longer t_{DAF} (not shown) decrease until they reach zero at $t_{DAF} \approx 121$ μs. Further increase of t_{DAF} leads to absorptive (positive) ENDOR spectra. However, no changes in line positions and no additional asymmetry of line shapes in the Davies ENDOR spectra were observed. Therefore, it is concluded that during this time a spin redistribution in the $A_1^{\bullet-}$ radical does not take place in PS I.

In order to compare the results of VMT ENDOR experiments with other methods for the determination of the signs of the hf couplings, a TRIPLE experiment was also performed on the RP at the same position of the magnetic field (with the pumping frequency set on the maximum of the high-frequency transition of the methyl group). The accumulation time was similar to that of the ENDOR experiment. However, difference TRIPLE signals were not observed. TRIPLE experiments with longer accumulation time were not performed on the RP.

For the kinetic modeling the relaxation parameters of the RP have to be obtained. Figure 5a presents the dependence of the two-pulse Hahn echo on t_{DD} (here $t_{DD} \approx t_{DAF}$) and the dependence of the inversion recovery three-pulse ex-

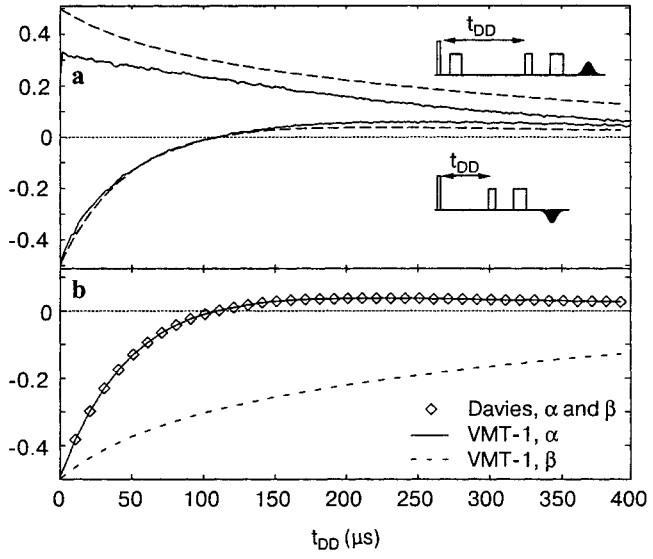

Fig. 5. a Experimental dependence of the echo intensity of the three-pulse inversion recovery and the two-pulse echo measurements of the spin polarized RP $P_{700}^{\bullet+}A_1^{\bullet-}$ in PS I on t_{DD} (solid lines), and corresponding simulations (dashed lines), see text. Time traces were recorded at a magnetic field close to g_x^Q (Fig. 3a). The echo detection sequence and the length of the inversion pulse are the same as in the Davies ENDOR sequence. Experimental traces are normalized on the amplitude of the simulation of the two-pulse echo at $t_{DD} = 0$ μs. The normalization factors for the two-pulse Hahn echo and the inversion recovery experiments are kept the same. The parameters of the simulations are Boltzmann factor of 0.98 (34 GHz, $T = 80$ K), $\tau_{RP} = 30$ μs, $T_{1e} = 130$ μs, $T_n = \infty$, $T_x = \infty$. **b** Simulation of Davies ENDOR and VMT-1 ENDOR signal intensities as a function of t_{DD}. The simulation parameters are the same as those for the results of panel a. In the Davies ENDOR sequence (◇) the intensities of ENDOR signals in the α and β electronic manifolds are the same.

periment on t_{DD} ($t_{DAF} = 1$ μs). Directly after the laser flash the intensity of the signal of the two-pulse sequence is negative (emissive signal), rapidly approaches and crosses zero and then decays slowly. This clearly shows the presence of two relaxation times in the decay. In contrast to the two-pulse echo dependence, the inversion recovery signal is always positive and exhibits mostly a decay with the slow relaxation rate. The fit of both dependences is presented in Fig. 5a (dashed lines). For fitting the formulae $\vec{n}(t_{DD} \approx t_{DAF}) = \exp[-(\Gamma + \Gamma_{RP})t_{DAF}]\vec{n}_0$ and Eq. (4a) have been used for the two-pulse echo and inversion recovery sequences, respectively. The intensity of the signal is obtained by $I_{EPR} = n_1 - n_2$. The Boltzmann factor f_B for the fits was taken to be equal to 0.98 (34 GHz, $T = 80$ K). Nuclear and cross-relaxation times were assumed to be significantly longer than the time of the experiment. From the fit of the experimental time traces the spin-relaxation time T_{1e} was determined to be 130 μs and the RP lifetime (charge recombination time) 30 μs. The use of $\tau_{RP} > T_{1e}$ did not allow a reasonable fitting of the two-pulse echo and inversion recovery traces. This also holds for the fitting of the intensities in the Davies ENDOR and the VMT

ENDOR spectra recorded at various delay times (see discussion below). The application of the MW inversion pulse in the beginning of the inversion recovery sequence and the VMT ENDOR sequences obviously prolongs the experimentally observed "lifetime" of the RP. This effect is well known in photosynthetic RCs [36, 40–43]. The inversion MW pulse transfers population from the α-manifold (partially singlet) to the β-manifold (pure triplet), from which recombination cannot take place. Thus, in this case the decay of the RP is limited by the spin-relaxation time T_{1e}.

The spin-relaxation time $T_{1e} = 130$ μs and the RP lifetime $\tau_{RP} = 30$ μs determined above are close to those found in previous X-band studies [41, 42, 44]. The charge recombination time measured by optical methods is considerably longer (around 150–200 μs) [45, 46]. The interpretation of the times and the discrepancy of the data obtained using EPR spectroscopy and data obtained using optical methods is still a subject of discussion and is outside the scope of this work (see, e.g., ref. 44). However, within our suggested model a constant spin-relaxation time $T_{1e} = 130$ μs and the RP lifetime $\tau_{RP} = 30$ μs allow us to explain all experimental results. Despite the somewhat larger intensity of the simulated inversion recovery signal as compared to the experiment (Fig. 5a), we consider the agreement between simulation and experiment satisfactory. One of the reasons for the overestimation of the inversion recovery signal amplitude might originate from the experimental conditions. For example, the spectral width of the applied inversion pulse is significantly narrower than the EPR line width, which can lead to incomplete excitation of the EPR spectrum.

Using the relaxation parameters determined above, the dependence of the Davies ENDOR intensity on t_{DD} was calculated according to Eqs. (2) and (3) (Fig. 5b, diamonds). Note that the intensities of the transitions in the α and β manifolds are identical. The ENDOR signal intensity decreases with a rate close to $1/\tau_{RP}$, crosses zero near 110 μs and then becomes positive. After that, the signal decays with a time constant close to T_{1e}. These results match the experimental observations.

The intensities of VMT-1 ENDOR lines were calculated using Eq. (3) and (4). The time dependence of the lines originating from the α and β manifolds is presented in Fig. 5b with dashed and solid lines, respectively. It is easy to see that the intensity of the transition in the α manifold (partially singlet) behaves similar to the one in the Davies ENDOR experiment, while its counterpart in the β manifold (pure triplet) decays much slower. It is this effect that creates the observed asymmetry of the lines intensities in the VMT spectra ("VMT effect").

Therefore, by comparing Davies and VMT ENDOR spectra it is possible to determine the electron spin manifold from which the ENDOR line originates. In particular, the lines belonging to the electronic α manifold show a very strong dependence on t_{DD} (decrease in amplitude and even change in polarization), while their counterparts from the β manifold stay mostly unchanged.

For the weak hf coupling case ($|A/2| < \nu_L$) considered in this article and a nucleus with positive g-factor (for ^{1}H, $g_H = +5.585691$), the line from the elec-

tronic α manifold has a frequency smaller than the Larmor frequency and the line from the β manifold has a larger one if the hfcc is positive and vice versa for a negative hfcc (Fig. 2c). For nuclei with negative *g*-factor the position of the ENDOR lines is reversed. Consequently, combining the information about the electronic manifold of the ENDOR line and the mutual positions of the lines from the α and β manifolds, the absolute sign of hf coupling can be determined (assuming that the sign of the nuclear *g*-factor is known).

The methodology discussed above can be directly applied for the analysis of the ^{1}H ENDOR spectra presented in Fig. 4. For example, the intensity of line 1 is decreased when t_{DD} is increased, which shows that this line originates from the nuclear transitions in the α ($|2\rangle$) electron manifold (compare Fig. 4a and Fig. 4c). Thus, the respective hfcc is positive. This coincides with the assignment of these lines to the methyl group protons, which have a positive hfcc [38, 47]. Another pronounced ENDOR line pair 3/3′ shows the opposite behavior: the intensity of line 3′ decreases when t_{DD} is increased, while the intensity of line 3 stays essentially constant. This behavior predicts a negative sign of the respective hfcc. This suggests that the line pair 3/3′ originates either from α-protons of the benzoic ring or the H-bond to VK_1 (see Fig. 4d for the expected signs of hfcc of different protons of VK_1). By this method, the signs of the hfccs for all lines exhibiting the VMT effect can be determined (Fig. 4c).

The VMT sequence can also be utilized to increase the spectral resolution by suppression of the ENDOR signals from the α manifold of the electron. This can be achieved by selection of a certain t_{DD} at which the intensity of the VMT signals from the α manifold is equal to zero. For example, a partial suppression of the α manifold signals is obtained in the VMT spectra recorded at t_{DD} = 134 μs (Fig. 4c). In this spectrum three sharp lines 5, 6, and 8 arising from negative hfccs are separated from the broad lines 4′ and 7′, which originate from the protons with positive hfcc. The lines from protons with negative hfcc are mostly visible at the low-frequency side, while the lines from the protons with positive couplings are visible on the high-frequency side of the spectrum.

A different type of VMT ENDOR experiment (VMT-2 ENDOR) is presented in Fig. 1. This experiment has parameters similar to the VMT-1 ENDOR experiment. However, the mixing time is introduced before the RF pulse, thus this pulse is shifted towards the detection sequence. This sequence was typically employed as a reference for the VMT-1 ENDOR experiment in ref. 18 (though not explicitly mentioned there). Using the approach presented above, it can be shown that for the case of thermal equilibrium (as in ref. 18) the result of the VMT-2 ENDOR sequence is similar to the Davies ENDOR sequence. However, our calculations show that in case of the polarized RP the VMT-2 ENDOR gives results similar to the VMT-1 ENDOR sequence and thus cannot be used as a reference. This is also found experimentally (data not shown).

The simplified kinetic model presented above can be extended to the complete system. Using the same experimental conditions, the extended model delivers essentially the same results. However, it can be shown that under different conditions, for example, in the strong coupling case or for significant over-

lap of the emissive and absorptive EPR lines, the VMT effect can vanish. Consequently, the experimental conditions chosen in this work are necessary for the observation of the VMT effect. Similarly to the observation of the VMT effect on the low-field edge of the RP EPR spectra (orientation close to g_x of $A_1^{\bullet-}$), one can expect to see a VMT effect also on the high-field edge. However, since the g_z values of $P_{700}^{\bullet+}$ and $A_1^{\bullet-}$ are very close to each other, significantly higher magnetic fields will be necessary.

For simplicity of the model described above, the nuclear and cross-relaxation processes were not considered. However, as was shown before, these processes can influence the kinetics of the VMT experiment [18] and the respective relaxation times can be determined. This may provide additional insight into the dynamics of the RP.

5 Conclusions

In this article, we have presented a method to determine the absolute signs of hf couplings in polarized RP ENDOR spectra. The VMT method allows the separation of ENDOR transitions originating from different electron spin manifolds by their dependence on the time parameters of the pulse sequence. In addition, the VMT sequence provides the possibility for a selective suppression of signals from one electron spin manifold and for the study of nuclear and cross-relaxation times. The kinetic model of Timmel et al. [36] adapted to the VMT experiment (fast decay of the RP states with singlet character, and significantly slower electron spin–lattice relaxation T_{1e}) provides the basis for explaining the observed effect in our experiments. The method has a very high sensitivity and does not require additional equipment. It can be applied in future experiments performed on photoinduced radicals and RPs [48] to determine the signs of the hfcc of protons and other magnetic nuclei to help in their assignments and to complete the spectroscopic information about the hf structure and spin density distribution. The method is expected to be of particular value in high-field ENDOR studies of such systems where a good orientational resolution is obtained for frozen solutions and powder samples.

Acknowledgments

This work is dedicated to Klaus Möbius (Freie Universität Berlin) and Kev Salikhov (Zavoisky Physical-Technical Institute, Russian Academy of Sciences, Kazan) on the occasion of their 70th birthdays. We are grateful to P. Fromme (Arizona State University, USA), J. Kern and J. Frank (TU Berlin, Germany) for providing trimeric PS I complexes isolated from the thermophilic cyanobacterium *T. elongatus*. We thank G. Klihm for technical assistance and K. M. Salikhov for providing the RP EPR simulation program. Generous funding by Max Planck Society and Deutsche Forschungsgemeinschaft (Sfb 663, TP A7) is gratefully acknowledged. M.L.A. was partially funded by the Sfb 498 (TP A3).

References

1. Feher G.: Phys. Rev. **103**, 834–835 (1956)
2. Möbius K., Plato M., Lubitz W.: Phys. Rep. **87**, 171–208 (1982)
3. Kurreck H., Kirste B., Lubitz W.: Electron Nuclear Double Resonance Spectroscopy of Radicals in Solution: Applications to Organic and Biological Chemistry. New York: VCH 1988.
4. Schweiger A., Jeschke G.: Principles of Pulse Electron Paramagnetic Resonance. New York: Oxford University Press 2001.
5. Lubitz W. in: Electron Paramagnetic Resonance, vol. 19, pp. 174–242. Specialist Periodical Reports. Cambridge: Royal Society of Chemistry 2004.
6. Bittl R., Zech S.G., Teutloff C., Krabben L., Lubitz W. in: Photosynthesis: Mechanisms and Effects (Garab G., ed.), pp. 509–514. Dordrecht: Kluwer Academic 1998.
7. Bittl R., Zech S.G.: Biochim. Biophys. Acta **1507**, 194–211 (2001)
8. Fursman C.E., Teutloff C., Bittl R.: J. Phys. Chem. B **106**, 9679–9686 (2002)
9. Teutloff C., Bittl R., Lubitz W.: Appl. Magn. Reson. **26**, 5–21 (2004)
10. Poluektov O.G., Utschig L.M., Dubinskij A.A., Thurnauer M.C.: J. Am. Chem. Soc. **126**, 1644–1645 (2004)
11. Carrington A., McLachlan A.D.: Introduction to Magnetic Resonance with Applications to Chemistry and Chemical Physics. New York: Harper & Row 1969.
12. Gerson F., Huber W.: Electron Spin Resonance Spectroscopy of Organic Radicals. New York: Wiley InterScience 2003.
13. Cook R.J., Whiffen D.H.: Proc. Phys. Soc. London **84**, 845–848 (1964)
14. Biehl R., Plato M., Möbius K.: J. Chem. Phys. **63**, 3515–3522 (1975)
15. Mehring M., Höfer P., Grupp A.: Ber. Bunsen-Ges. Phys. Chem. **91**, 1132–1137 (1987)
16. Epel B., Goldfarb D.: J. Magn. Reson. **146**, 196–203 (2000)
17. Möbius K., Lubitz W., Plato M. in: Advanced EPR: Applications in Biology and Biochemistry (Hoff A.J., ed.), pp. 441–499. Amsterdam: Elsevier 1989.
18. Epel B., Pöppl A., Manikandan P., Vega S., Goldfarb D.: J. Magn. Reson. **148**, 388–397 (2001)
19. Epel B., Manikandan P., Kroneck P.M.H., Goldfarb D.: Appl. Magn. Reson. **21**, 287–297 (2001)
20. Davies E.R.: Phys. Lett. A **47**, 1–2 (1974)
21. Thurnauer M.C., Brown J.W., Gast P., Feezel L.L.: Radiat. Phys. Chem. **34**, 647–651 (1989)
22. Bock C.H., Van der Est A., Brettel K., Stehlik D.: FEBS Lett. **247**, 91–96 (1989)
23. Jordan P., Fromme P., Witt H.T., Klukas O., Saenger W., Krauss N.: Nature **411**, 909–917 (2001)
24. Fromme P., Witt H.T.: Biochim. Biophys. Acta **1365**, 175–184 (1998)
25. Sienkiewicz A., Smith B.G., Veselov A., Scholes C.P.: Rev. Sci. Instrum. **67**, 2134–2138 (1996)
26. Epel B., Gromov I., Stoll S., Schweiger A., Goldfarb D.: Concepts Magn. Reson. B **26**, 36–45 (2005)
27. Salikhov K.M., Schlüpmann J., Plato M., Möbius K.: Chem. Phys. **215**, 23–35 (1997)
28. Kandrashkin Y.E., Salikhov K.M., Van der Est A., Stehlik D.: Appl. Magn. Reson. **15**, 417–447 (1998)
29. Hore P.J. in: Advanced EPR: Applications in Biology and Biochemistry (Hoff A.J., ed.), pp. 405–440. Amsterdam: Elsevier 1989.
30. Buckley C.D., Hunter D.A., Hore P.J., McLauchlan K.A.: Chem. Phys. Lett. **135**, 307–312 (1987)
31. Closs G.L., Forbes M.D.E., Norris J.R.: J. Phys. Chem. **91**, 3592–3599 (1987)
32. Hore P.J., Hunter D.A., McKie C.D., Hoff A.J.: Chem. Phys. Lett. **137**, 495–500 (1987)
33. Bittl R., Kothe G.: Chem. Phys. Lett. **177**, 547–553 (1991)
34. Kothe G., Weber S., Bittl R., Ohmes E., Thurnauer M.C., Norris J.R.: Chem. Phys. Lett. **186**, 474–480 (1991)
35. Dzuba S.A., Bosch M.K., Hoff A.J.: Chem. Phys. Lett. **248**, 427–433 (1996)
36. Timmel C.R., Fursman C.E., Hoff A.J., Hore P.J.: Chem. Phys. **226**, 271–283 (1998)
37. Zech S., Hofbauer W., Kamlowski A., Fromme P., Stehlik D., Lubitz W., Bittl R.: J. Phys. Chem. B **104**, 9728–9739 (2000)
38. Rigby S.E.J., Evans M.C.W., Heathcote P.: Biochim. Biophys. Acta **1507**, 247–259 (2001)
39. Poluektov O.G., Utschig L.M., Dubinskij A.A., Thurnauer M.C.: J. Am. Chem. Soc. **127**, 4049–4059 (2005)
40. Salikhov K.M., Molin Y.N.: J. Phys. Chem. **97**, 13259–13266 (1993)
41. Iwaki M., Itoh S., Hara H., Kawamori A.: J. Phys. Chem. B **102**, 10440–10445 (1998)

42. Dzuba S.A., Hara H., Kawamori A., Iwaki M., Itoh S., Tsvetkov Y.D.: Chem. Phys. Lett. **264**, 238–244 (1997)
43. Dzuba S.A., Proskuryakov I.I., Hulsebosch R.J., Bosch M.K., Gast P., Hoff A.J.: Chem. Phys. Lett. **253**, 361–366 (1996)
44. Dzuba S.A., Kawamori A., Katsuta N., Hara H., Mino H., Itoh S.: Chem. Phys. Lett. **362**, 307–313 (2002)
45. Brettel K.: Biochim. Biophys. Acta **1318**, 322–373 (1997)
46. Brettel K., Leibl W.: Biochim. Biophys. Acta **1507**, 100–114 (2001)
47. Epel B., Niklas J., Sinnecker S., Zimmerman H., Lubitz W.: J. Phys. Chem. B **110**, 11549–11560 (2006)
48. Stehlik D., Möbius K.: Annu. Rev. Phys. Chem. **48**, 745–784 (1997)

Authors' address: Wolfgang Lubitz, Max-Planck-Institut für Bioanorganische Chemie, Stiftstrasse 34-36, 45470 Mülheim an der Ruhr, Germany
E-mail: lubitz@mpi-muelheim.mpg.de